Generation and Evolution of Phononic Frequency Combs via Coherent Energy Transfer between Mechanical Modes

Jiangkun Sun,[1,2] Sheng Yu,[2] Hemin Zhang,[1] Dongyang Chen,[1] Xin Zhou,[2] Chun Zhao,[1] Dustin D. Gerrard,[3] Ryan Kwon,[3] Gabrielle Vukasin,[3] Dingbang Xiao,[2,*] Thomas W. Kenny,[3] Xuezhong Wu,[2] and Ashwin Seshia[1,†]

[1] *Nanoscience Centre, University of Cambridge, Cambridge CB3 0FF, United Kingdom*
[2] *College of Intelligence Science, National University of Defense Technology, Changsha 410073, China*
[3] *Department of Mechanical Engineering, Stanford University, Stanford, California 94305, USA*

(Received 12 November 2021; revised 12 August 2022; accepted 5 December 2022; published 10 January 2023)

Phononic frequency combs represent the mechanical analog of optical frequency combs. Several independent experimental studies have demonstrated the onset and evolution frequency comb response in a variety of micro- and nanoelectromechanical devices in recent years. A theoretical basis for exploring and understanding the conditions for comb generation and evolution with varying driving parameters is essential to enable future practical applications. Here, we present the comparison between modeling and experimental results on the generation and evolution mechanism of phononic frequency combs in a nonlinear micromechanical resonator from the perspective of coherent energy transfer between two mechanical modes. Phononic frequency combs emerge in a strong coupling regime involving nonlinear resonances when the amplitudes and phases of two coupled mechanical modes are modulated via coherent energy transfer. The spacing and number of comb teeth can be analytically estimated based on modeling the nature of the interaction of the coupled modes under the specified driving conditions. As the driving conditions are varied, the phononic frequency comb evolves into different forms and a phenomenological model for the system is established to accurately predict the evolution of phononic frequency combs. The alignment between experiment and model provides a basis for the engineering of this phenomenon in future device applications.

DOI: 10.1103/PhysRevApplied.19.014031

I. INTRODUCTION

A frequency comb is composed of a series of discrete, equally spaced lines in the spectrum. In the optical domain, photonic frequency combs have generated widespread interest due to their diverse applications spanning from frequency metrology [1–4], ultraprecision clocks [5,6], optical communications to quantum information processing [7–9]. To enable miniaturization and integration of photonic comb devices, dissipative Kerr solitons in coherently pumped high quality-factor optical microresonators have been extensively studied [10–15]. More recently, micromechanical devices have emerged as a platform for the generation of a phononic frequency comb (PFC). Multifrequency parametric mixing mediated via nonlinear mode coupling as a path towards PFC generation has previously been experimentally demonstrated in mechanical resonators [16–20]. Specifically, the phenomenon of internal resonance, which satisfies the commensurate relationship between resonant modes and can enable strong mode interaction with weaker signal levels has proved to be an effective way to generate PFCs [21]. For example, some previous studies have demonstrated the phenomenon of PFCs and explored the boundaries of Hopf bifurcations in a micromachined resonator [22,23]. However, a theoretical treatment of the experimental observations that accurately describe and predict the generation and evolution of PFCs demonstrating good alignment for the devices under test is essential to extend these observations towards practical applications. This paper establishes a key milestone towards this objective by developing a suitable dynamical model for an established microelectromechanical device that accurately captures experimental observations of internal resonance and PFC formation and evolution with varying drive conditions.

In this paper, we demonstrate the generation and evolution mechanism of a PFC in a micromachined disk resonator based on the strong nonlinear coupling of two mechanical modes through 1:2 internal resonance [24,25]. When one mode is driven by a single actuation signal,

*dingbangxiao@nudt.edu.cn
†aas41@cam.ac.uk

energy is continuously exchanged between the two resonantly coupled modes. It is noted that the coherent energy transfer transforms into periodic motion in the specific regime of the driving parameter space [26]. Simultaneously, these two mechanical modes will be modulated via coherent energy transfer, resulting in the generation of a PFC. Furthermore, the evolution of PFCs with varying driving conditions is also investigated. Finally, a theoretical model is established to explain and predict the generation and evolution of PFCs under different driving parameters, providing the basis for potential future application.

II. M-SHAPED RESPONSES UNDER INTERNAL RESONANCE

A microelectromechanical disk resonator is utilized as the experimental platform to demonstrate the coherent energy transfer between two mechanical modes. As shown in Fig. 1(a), the disk resonator supported by a central anchor is constructed of 45 concentric rings interconnected through spokes with 720 μm diameter and 40 μm thickness. There are 16 capacitive electrodes with 1.5-μm gaps for the differential actuation and detection of mechanical motion through a lock-in amplifier. A direct-current bias voltage $V_{\rm dc}$ is applied to the resonator's body. In addition, an alternating voltage with amplitude V_d and frequency Ω_d is also utilized to adjust the driving amplitude. Figure 1(b) illustrates the linear amplitude-frequency responses of two mechanical modes of interest when $V_{\rm dc} = 23.95$ V, $V_d = 1$ mV. The resonant frequencies of these two modes satisfy a proportional relationship close to two. Internal resonance is triggered when the nonlinear coupling of two modes is strong enough. As illustrated in Fig. 2(a), the forward and reverse frequency sweep is carried out under $V_{\rm dc} = 23.95$ V, $V_d = 20$ mV to characterize the nonlinear responses under internal resonance. However, the frequency sweep cannot map out all the fixed points due to the existence of multiple solutions for the same driving frequency. Hence, the closed-loop measurements are conducted using the phase-locked loop function of the lock-in amplifier to identify some fixed points, which can not be obtained from frequency sweeping by modifying the set phases [27].

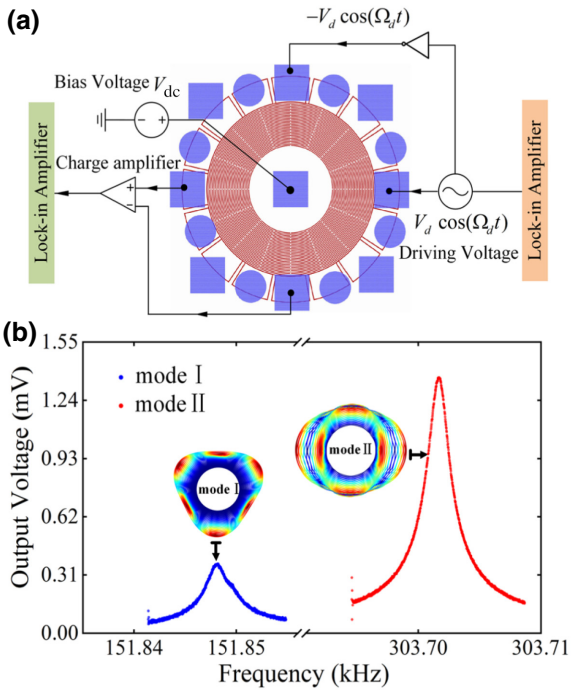

FIG. 1. The experimental platform. (a) A schematic of the experimental setup. (b) Characterization of two mechanical modes in the linear region.

To investigate the exotic M-shaped responses, a model of two coupled resonant modes is introduced to carry out the theoretical analysis under two-to-one internal resonance. After normalization and introducing a small parameter ϵ as explained in Appendix A, the equations governing this model can be expressed as

$$\begin{aligned} &\ddot{x} + \varepsilon\gamma_1\dot{x} + \omega_1^2 x + \varepsilon\alpha xy = \varepsilon f_x \cos(\omega_d t+\tau), \\ &\ddot{y} + \varepsilon\gamma_2\dot{y} + \omega_2^2 y + \varepsilon\beta x^2 = 0, \end{aligned} \tag{1}$$

where x, y are the amplitudes of modes I and II with the resonant frequencies of ω_1 and ω_2, respectively. γ_1, γ_2 and α, β are the damping rates and quadratic nonlinear coefficients of two modes, respectively. f_x and ω_d are the amplitude and frequency of the driving force applied to mode I.

The method of multiple scales is employed to model the M-shaped responses. Two tuning parameters $\epsilon\sigma_2 = \omega_2 - 2\omega_1$ and $\epsilon\sigma_1 = \omega_d - \omega_1$ are utilized to adjust the strength of internal resonance and driving frequency, respectively. As shown in Fig. 2(b), the simulated M-shaped response is able to explain the experimental results in Fig. 2(a) qualitatively. These two types of transition from stable to unstable motion can be characterized as saddle-node and Hopf bifurcations, respectively, as explained in Appendix A. As for the former, stable and unstable fixed points collide and annihilate each other, generating saddle-node bifurcations A, B, C, D and resulting in the jump phenomena in the frequency response. The other particular type of motion occurring in the regime between two Hopf bifurcations is the focus of this paper and is elaborated in greater detail below.

Numerical simulations and experiments are also carried out to characterize various M-shaped responses under different driving parameters. During these experiments, the bias voltage $V_{\rm dc}$ is used to tune the ratio of the resonance frequencies of the two modes to determine the strength of internal resonance σ_2 because these resonant frequencies

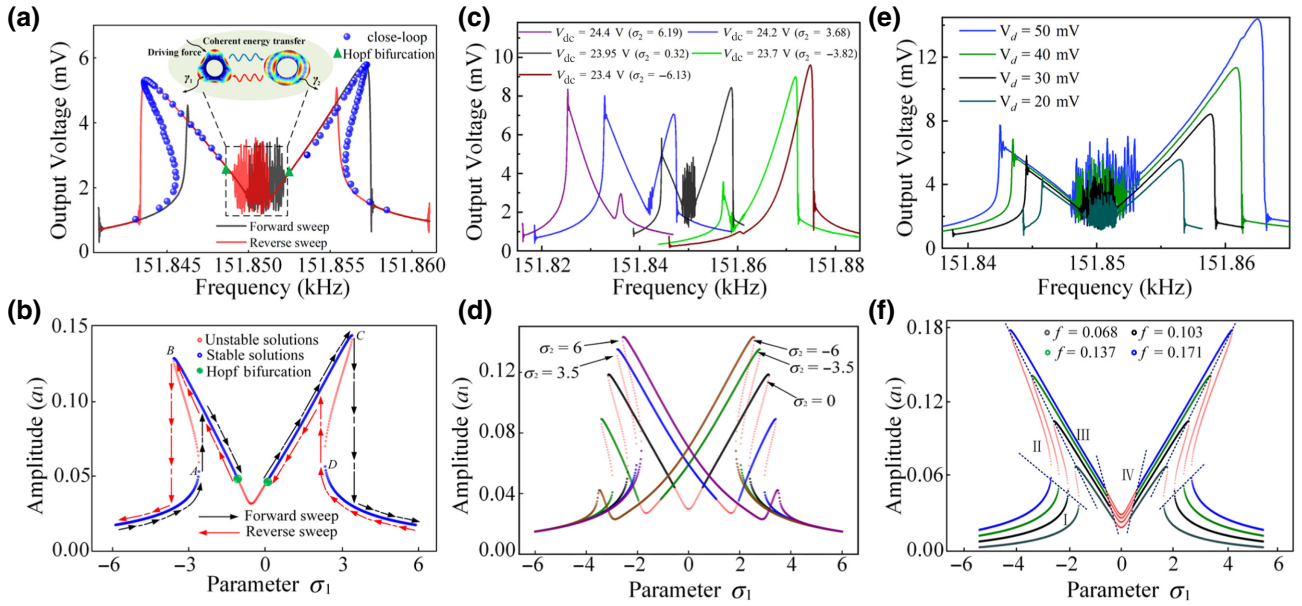

FIG. 2. (a) M-shaped response under internal resonance when $V_{\mathrm{dc}} = 23.95$ V, $V_d = 20$ mV. (b) Simulation results of M-shaped response. (c) Forward-sweep experimental results when driving amplitude $V_d = 30$ mV under different bias voltages V_{dc}. (d) Simulation results when driving amplitude $f = 0.11$ for varying σ_2. (e) Forward-sweep experimental results when bias voltage $V_{\mathrm{dc}} = 23.95$ V under different driving amplitudes. (f) Simulation results under different driving amplitudes f when $\sigma_2 = 0$.

have different frequency shifts due to the negative electrostatic stiffness under bias voltages (see Appendix A). Additionally, the driving voltage amplitude V_d and frequency Ω_d are varied to tune the amplitude and frequency of driving force, respectively. Only forward frequency sweeps are illustrated in those experimental results to demonstrate these exotic responses. As illustrated in Fig. 2(c) and (d), the simulation and experimental results under varying strength of internal resonance are consistent with each other. It is observed that σ_2 influences the amplitude ratio of the two peaks associated with the M-shaped response as predicted in the simulation. When the internal resonance is perfectly tuned ($\sigma_2 = 0$), the M-shaped response is symmetric and has modulated motions in the middle, which means that the strength of internal resonance is relatively strong. However, the absolute ratio of the two peaks in the M-shaped response increases and the modulated motions shift or even disappear when σ_2 is far away from zero, which indicates a weaker internal resonance. Similarly, the M-shaped responses under different driving amplitudes as shown in Figs. 2(e)–2(f) consist of four distinct regions including two stable regions I, III and two unstable regions II (jump phenomena), IV (modulated motions). Region IV between two Hopf bifurcations is the area that will be investigated more thoroughly in the following.

III. GENERATION MECHANISM OF PFC

Based on the Hopf bifurcation theorem, the two mechanical modes are expected to exhibit limit-cycle oscillations near the Hopf bifurcation. The associated modal motion does not equate to constant-amplitude vibration because energy is transferred forth and back coherently between these two mechanical modes. Hence, the fixed points and modulated motions in the M-shaped response represent different forms of energy transfer as shown in Fig. 2(a). When the resonator is driven at these fixed points by closed-loop actuation, energy initially imparted to mode I will be continuously transferred to mode II to reach a balance between external supply and dissipation of energy, thus maintaining the stable vibration of the two mechanical modes. However, for open-loop driving between two Hopf bifurcations, energy is pumped back and forth between these two mechanical modes continuously. This kind of energy transfer is enabled by the strong coupling between two mechanical modes through the quadratic nonlinearity underpinning the internal resonance observed here. Besides, external energy is continuously pumped into mechanical mode I by the driving force with amplitude V_d and frequency Ω_d. There is a balance between external energy and dissipation of the two mechanical modes to maintain the associated vibration. Besides, the coherent transfer of energy results in the modulation of two mechanical modes' amplitudes and phases at the same time.

To observe coherent energy transfer in the experiments, we still keep $V_{\mathrm{dc}} = 23.95$ V, $V_d = 20$ mV and choose a driving frequency $\Omega_d = 2\pi \times 151.852$ kHz between two Hopf bifurcations. After the demodulation of detection signal by Ω_d and $2\Omega_d$, it is observed that amplitudes of mode

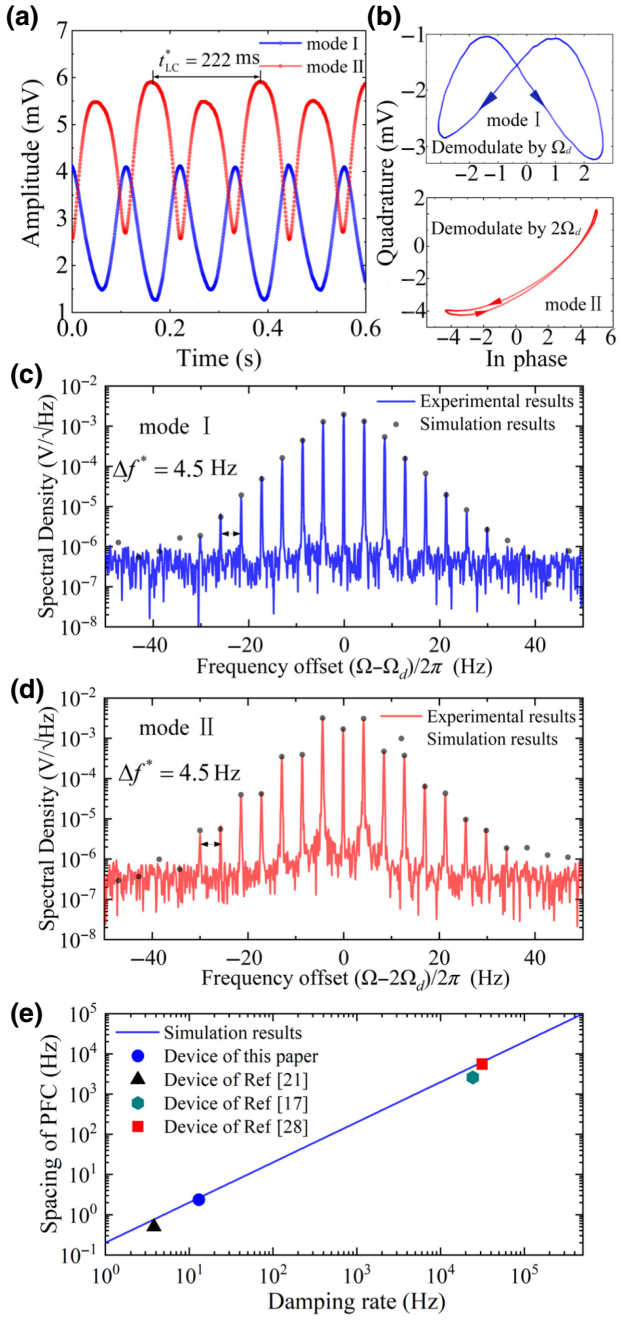

FIG. 3. Observation of coherent energy transfer under $V_{\rm dc} = 23.95$ V, $V_d = 20$ mV and $\Omega_d = 2\pi \times 151.8420$ kHz. (a) Illustration of coherent energy transfer. (b) Limit cycles of mode I and mode II, respectively. (c),(d) PFCs observed in the spectrum of two mechanical modes. (e) PFC frequency spacing as a function of damping rate for various devices.

I and mode II periodically vary out of phase with each other due to the coherent energy transfer between two modes as shown in Fig. 3(a). Besides, the in-phase and quadrature components of two mechanical modes constitute two limit cycles as shown in Fig. 3(b). Although the periods of the two limit cycles are the same, their shapes are different because these two mechanical modes have different responses under coherent energy transfer. In addition, the period and shape of the limit cycle are related to the rate and form of coherent energy transfer between two mechanical modes, respectively. When we observe the experimental results above in the frequency spectrum, there are two different PFCs in two mechanical modes as shown in Figs. 3(c) and 3(d). It is also noted that the period $t^*_{\rm LC}$ of coherent energy transfer determines the comb spacing $\Delta f^* = 1/t^*_{\rm LC} = 4.5$ Hz of PFCs in the frequency spectrum. Hence, the observed PFCs of two mechanical modes have the same spacing. The amplitudes of combs are not the same due to the different phase and amplitude modulations for the two mechanical modes.

Theoretical analysis is also carried out to reveal the generation mechanism of PFCs. The vibration signal of mechanical mode I demonstrates a periodic phase and amplitude modulation that can be expressed as

$$x(t) = a(t)\cos[\omega_d t + \theta(t)] \approx \sum_{m=-\infty}^{\infty} \Gamma_m \cos((\omega_d + m\Delta\omega)t + \Theta_m), \qquad (2)$$

where $\Delta\omega = 2\epsilon\pi/T_{\rm LC}$, $a(t)$ and $\theta(t)$ are amplitude and phase periodic modulation functions of mode I, respectively, with the same period $T_{\rm LC}$. Γ_m is the amplitude of mth comb line. The detailed derivation of Eq. (2) is demonstrated in Appendix B.

The expression of Eq. (2) shows equally spaced discrete sidebands around the frequency Ω_d of mode I representing PFCs in the frequency domain. The simulation is also carried out to obtain the spacing and amplitude of the mth comb tooth Γ_m by substituting the experimental results of $a(t)$ and $\theta(t)$ into Eq. (2). The good alignment between simulation and experimental results verifies the generation mechanism of PFCs illustrated in Figs. 3(c) and 3(d).

According to the method of multiple scales, the relationship between the time scales T_1 of the limit cycle and the real time t^* can be expressed as $T_1 = \varepsilon t = \varepsilon\omega_0 t^* = \gamma t^*$ where $\gamma = (\gamma_X + \gamma_Y)/2$ represents the averaged damping rate. Therefore, a limit cycle with the period of $T_{\rm LC}$ under the time scales T_1 will generate the PFC with the spacing of $\Delta f^* = 1/t^*_{\rm LC} = \gamma/T_{\rm LC}$. Thus, the modifying orders of magnitude of the damping rates has no influence on the forms and parameters of Eq. (A4), as well as the period $T_{\rm LC}$ of limit cycles. It means that the magnitude of the comb spacing is determined by damping rates across different phononic devices as shown in Fig. 3(e). In other words, the order of magnitude of the comb spacing representing the rate of coherent energy transfer depends on the damping rate of micromachined resonator. Hence, we can obtain different magnitudes of comb spacing from Hz to MHz by varying the damping rates. The conclusions and theoretical analysis are consistent with previously reported

work [17,21,28], which provides a valuable guideline for the design of future PFC devices.

IV. EVOLUTION MECHANISM OF PFC

The underlying mechanism for the generation of PFCs is demonstrated under a specific driving parameter above. However, the PFC evolves into different forms along with the variation of driving frequency in region IV [Fig. 2(f)] of modulated motions. When the driving frequency varies between two Hopf bifurcations, the rate and form of coherent energy transfer depending on the nonlinear dynamics would vary accordingly. As illustrated in Fig. 4(a), the evolution of PFCs in region IV demonstrates abundant characteristics with the varying driving frequency Ω_d. To be specific, there is only one spectral line in PFC I before the Hopf bifurcation. However, the self-induced oscillations arise through Hopf bifurcation and result in coherent energy exchange between the two mechanical modes and the formation of PFCs [29,30]. Following the route of increasing driving frequency, the spacing of combs Δf^* varies with the exchange period of coherent energy transfer between two mechanical modes. There are several singular features observed in the process of evolution, which interrupt the normal evolution process and reshapes the resulting spectral responses. For example, the number of comb teeth in PFC III suddenly doubles when a period-doubling bifurcation takes place. It is also noteworthy that a chaotic response emerges in the route of evolution when period-doubling cascades occur [31,32]. It is also observed that PFC IV has a continuous broad-band character, which means that the coherent energy transfer occurs in a chaotic manner [33,34]. To explain the evolution characteristics of PFCs, the bifurcation diagram and corresponding Lyapunov exponents are calculated from the theoretical model to identify the nonlinear dynamics as shown in Fig. 4(d). It is very clear from the simulation results that a chaotic motion also emerges from a periodic motion via a sequence of period-doubling bifurcations by varying the driving frequency. Moreover, it is also observed that some individual

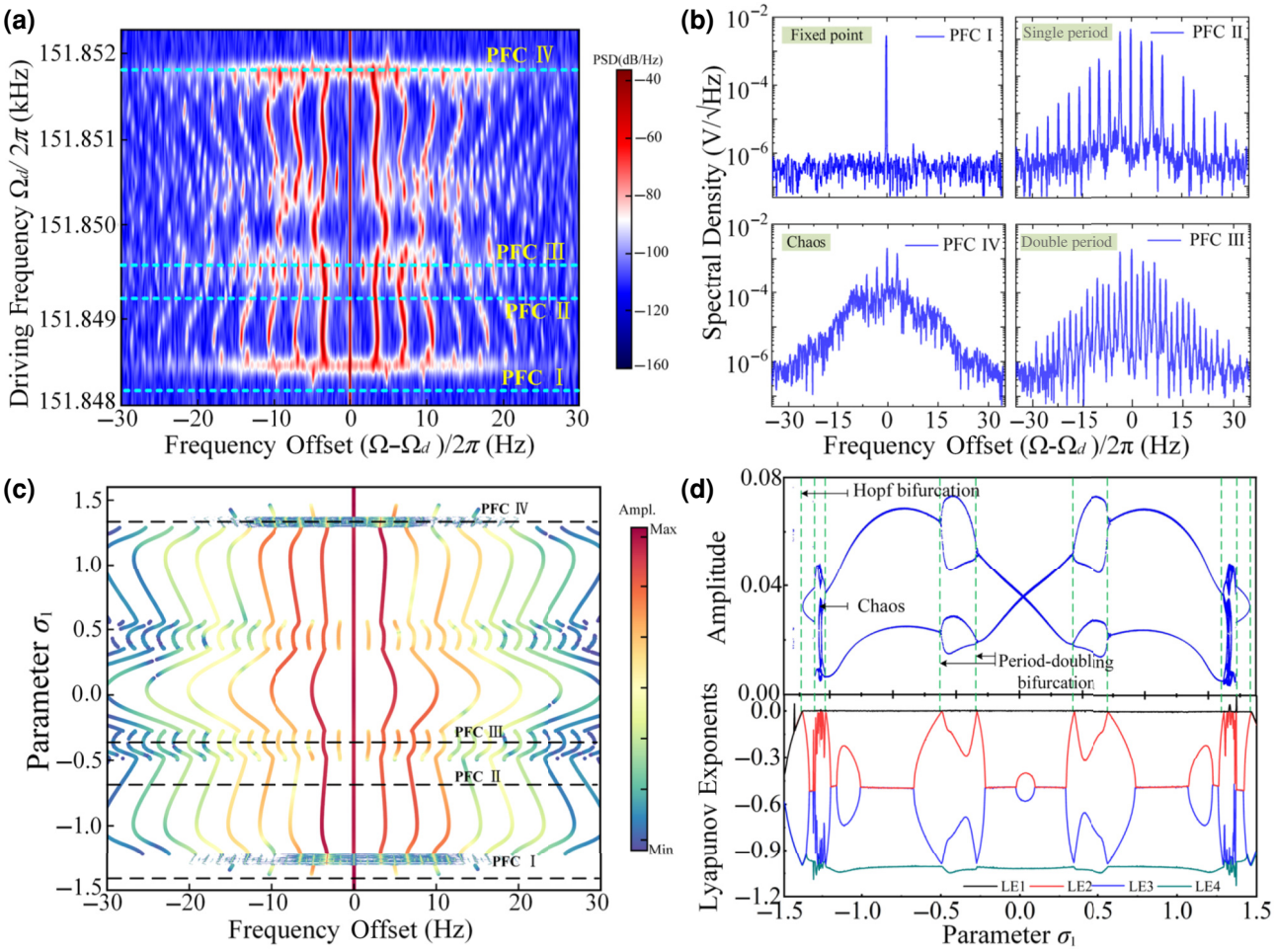

FIG. 4. (a) The evolution of PFCs under $V_{dc} = 23.95$ V, $V_d = 30$ mV. (b) Frequency spectra of specific types of PFCs. (c) Simulation results illustrating of PFC evolution for $\sigma_2 = 0$. (d) Bifurcation diagram and Lyapunov exponents from the model.

period-doubling bifurcations occur in the process of evolution, not resulting in chaotic motion but the number of comb teeth doubling or halving as shown in Fig. 4(a).

As previously outlined a model is developed to describe nonlinear modal coupling leading to the appearance and evolution of frequency comb response. To carry out numerical simulations based on this model, the parameters of the theoretical model are fitted from the experimental results of M-shaped responses (see Appendix A). First, chaotic and regular motions are distinguished from the Lyapunov exponents to accurately predict the evolution of PFCs. When the regimes of chaotic motion and bifurcations are identified, the comb spacing of PFCs in the residual regimes changes continuously with the modification of the driving frequency. It means that the forms of energy transfer between two mechanical modes gradually vary at the same time. Apart from chaotic motion and bifurcations, the shooting method is applied to the theoretical model to identify the period of energy transfer [35] and the comb spacing can be obtained as $\Delta f^* = 1/t^*_{\mathrm{LC}}$ simultaneously. The amplitudes of comb teeth can also be calculated from the in-phase and quadrature components of limit cycles based on Eq. (2). In this way, a single PFC under a certain driving frequency can be determined from the theoretical model. Then the continuation method is utilized to investigate the PFC evolution, namely the variation of comb spacing and amplitudes along with the continuous modification of driving parameters. To be more specific, the continuation algorithm computes a consecutive sequence of limit cycles with various periods and shapes under the variation of driving frequency to demonstrate different forms of coherent energy transfer [36]. Combining these PFCs and singular features such as bifurcations and chaos in the direction of driving frequency variation, we can obtain the simulation results illustrating the evolution of PFCs. As illustrated in Fig. 4(c), the simulation and experimental results are consistent with each other to demonstrate the evolution of PFCs when the internal resonance is perfectly tuned ($\sigma_2 = 0$).

In summary, coherent energy transfer between the two mechanical modes is determined by the nonlinear coupling strength and driving frequency. The nonlinear coupling strength of this internal resonance system is directly determined by dc bias V_{dc} and driving amplitude V_d. To be specific, V_{dc} is utilized to adjust the strength of internal resonance σ_2 and the driving amplitude V_d is varied to tune the resonant amplitude of two mechanical modes. In order to investigate the evolution laws for PFCs thoroughly, experiments are carried out to demonstrate the evolution of PFCs under different driving parameters as illustrated in Fig. 5. Setting the driving amplitude V_d as 20 mV, the evolution under different V_{dc} has various characteristics. When dc bias $V_{\mathrm{dc}} = 23.8$ V ($\sigma_2 = -2.55$), there is an obvious divergent trend in the process of evolution after the chaotic motion, which means that the comb spacing increases with increasing driving frequency and the coherent energy transfer rate is gradually becoming larger. In contrast, a convergent trend is observed in the evolution of PFCs under $V_{\mathrm{dc}} = 24.1$ V ($\sigma_2 = 2.5$) and indicates that the coherent energy transfer rate is gradually becoming smaller. Therefore, these two cases demonstrate the opposite trends for the PFC evolution under the opposite strength of internal resonance σ_2. As for the dc bias $V_{\mathrm{dc}} = 23.95$ V ($\sigma_2 = 0.21$), the evolution has no divergent or convergent trend and describes the symmetrical trends along with the increasing driving frequency. As the driving amplitude V_d increases, the frequency ranges between two Hopf bifurcations are expanded as shown in Figs. 2(e)–2(f). The convergent and divergent trends can still be observed in the evolution of PFCs under $V_{\mathrm{dc}} = 24.1$ V and $V_{\mathrm{dc}} = 23.8$ V, respectively, when driving amplitude V_d increases to 30 mV as shown in Figs. 5(d) and 5(f). Besides, the evolution of PFCs under $V_{\mathrm{dc}} = 23.95$ V still maintains a symmetrical trend. Comparing the experimental results when V_d is equal to 20 and 30 mV under the same V_{dc}, more bifurcations and chaos emerge in the process of evolution. This is because the coupling strength of two mechanical modes increases with the rising of driving amplitude V_d and the nonlinear dynamics between two Hopf bifurcations are becoming richer.

The experiments of the forward evolution from left to right Hopf bifurcations and reverse evolution from right to left Hopf bifurcations are also investigated. The experimental results of forward and reverse evolution are the same when V_d is relatively small. However, it is observed that the evolution under $V_{\mathrm{dc}} = 23.95$ V and $V_d = 50$ mV loses its symmetry in the direction of driving frequency due to the emergence of the extra evolution parts separated by the dash black lines as shown in Figs. 5(g) and 5(h). This asymmetry is caused by the bistable behaviors in this evolution regime because the nonlinear coupling of two mechanical modes is really strong when the drive amplitude is increased to 50 mV. To be specific, the forward evolution starts with fixed points and finished with limit cycles. This is in contrast to the reverse evolution representing different forms of energy transfer in the frequency regimes beyond the dashed black lines. Combining the forward and reverse evolution together, we obtain a complete evolution process under this circumstance to demonstrate the nonlinear dynamics and it can be also explained in the simulation results as illustrated in Fig. 5(i). This hysteresis phenomenon of the PFC presents evidence for nonunique frequency comb solutions for specific driving conditions under strong nonlinear coupling, which is also previously reported [37].

Above all, the evolution characteristics of PFCs depend on the strength of internal resonance σ_2 and the richness of evolution is related to the driving amplitudes. All the qualitative trends of experiments above can be predicted accurately by the theoretical model as shown in

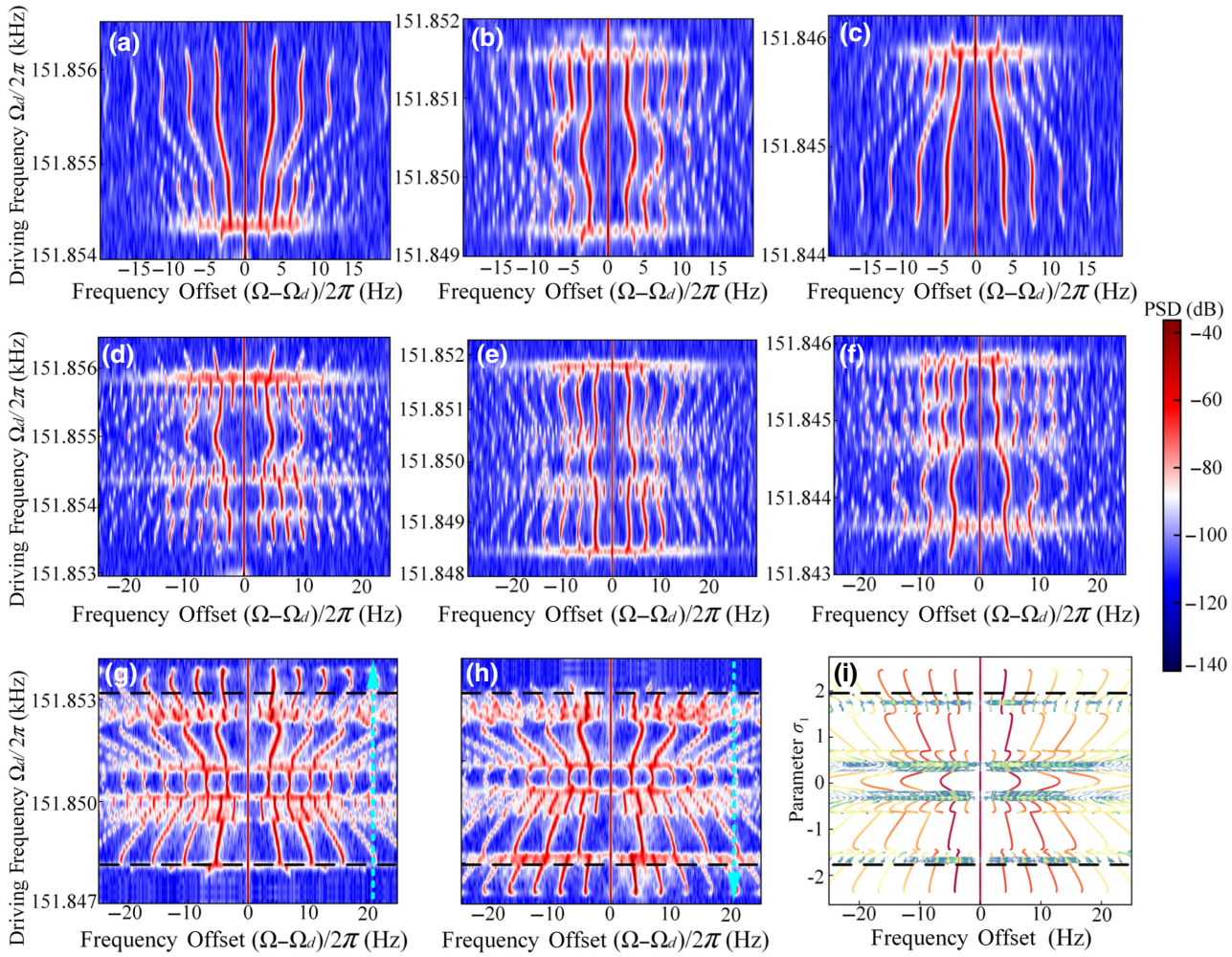

FIG. 5. A series of PFCs' evolution under different driving parameters. (a) $V_d = 20$ mV, $V_{\rm dc} = 23.8$ V ($\sigma_2 = -2.55$). (b) $V_d = 20$ mV, $V_{\rm dc} = 23.95$ V ($\sigma_2 = 0.21$). (c) $V_d = 20$ mV, $V_{\rm dc} = 24.1$ V ($\sigma_2 = 2.5$). (d) $V_d = 30$ mV, $V_{\rm dc} = 23.8$ V ($\sigma_2 = -2.55$). (e) $V_d = 30$ mV, $V_{\rm dc} = 23.95$ V ($\sigma_2 = 0.21$). (f) $V_d = 30$ mV, $V_{\rm dc} = 24.1$ V ($\sigma_2 = 2.5$). (g) Experimental results of forward evolution under $V_{\rm dc} = 23.95$ V, $V_d = 50$ mV. (h) Experimental results of reverse evolution under $V_{\rm dc} = 23.95$ V, $V_d = 50$ mV. (i) Simulation results under $V_{\rm dc} = 23.95$ V and $V_d = 50$ mV.

Appendix C. The slight differences between experimental and simulation results, especially for the amplitudes of comb teeth, mainly come from parameter fitting errors associated with the theoretical model. The effectiveness of the theoretical model is verified by the consistency of experimental and simulation results and provides us with the ability to predict and manipulate the evolution of PFCs under various driving parameters.

In this study, we reveal the generation mechanism of PFCs from a perspective of coherent energy transfer between two mechanical modes. The amplitudes and phases of the two modes are periodically modulated by continuous coherent energy exchange and PFCs can be observed in the frequency spectrum. Additionally, a dynamical model is established to predict the spacing and amplitudes of the PFC. Furthermore, the evolution of PFCs between two Hopf bifurcations under different driving amplitudes and strength of internal resonance are also investigated experimentally and theoretically. The theoretical analysis of the generation mechanism provides useful guidance for the future design of PFC devices. A number of potential applications of PFCs are currently being investigated and the results reported here will find applicability to these and other related investigations including to physical sensors [38], multichannel acoustic ranging [39], fundamental investigations of phonon manipulation and phonon computing by tuning different driving parameters [40,41], and vibration energy harvesting [42].

ACKNOWLEDGMENTS

The authors thank Milind Pandit, and Madan Parajuli for helpful discussions and assisting with training

on laboratory equipment. This work is partly supported by the National Key R&D Program of China (2018YFB2002304), MEMS Engineering Center of Hunan and the Laboratory of Science and Technology on Integrated Logistics Support. This work is also supported in part by the UK Engineering and Physical Sciences Research Council under Grant No. EP/P013848/1.

APPENDIX A: NONLINEAR COUPLING MODEL

1. Basic equations of nonlinear model

The initial model of two coupled resonant modes under two-to-one internal resonance is introduced as follows:

$$\ddot{X} + \gamma_X \dot{X} + \omega_X^2 X + \alpha_X XY = F_X \cos(\Omega_d t^* + \tau),$$
$$\ddot{Y} + \gamma_Y \dot{Y} + \omega_Y^2 Y + \beta_Y X^2 = 0, \tag{A1}$$

where X, Y are the responses of two mechanical modes with the frequencies of $\omega_X = 2\pi f_1$ and $\omega_X = 2\pi f_2$, respectively, which satisfies $\omega_X : \omega_Y \approx 1:2$ as two-to-one internal resonance. γ_X, γ_Y, and α_X, β_Y are the damping rates and nonlinear coupling coefficients of two modes, respectively.

The method of multiple scales, as presented by Nayfeh, can be employed to describe the response. We introduce dimensionless variables $t = \omega_0 t^* (\omega_0^2 = (\omega_X^2 + \omega_Y^2)/2)$, $x = X/d_0$, and $y = Y/d_0$, where t^* denotes the real time, d_0 is the initial capacitive gap. By introducing the small parameter $\epsilon = \gamma/\omega_0$ and $\gamma = (\gamma_X + \gamma_Y)/2$, Eq. (1) can be normalized as

$$\ddot{x} + \varepsilon\gamma_1 \dot{x} + \omega_1^2 x + \varepsilon\alpha xy = \varepsilon f_x \cos(\omega_d t + \tau)$$
$$\ddot{y} + \varepsilon\gamma_2 \dot{y} + \omega_2^2 y + \varepsilon\beta x^2 = 0 \tag{A2}$$

where $\omega_1 = \omega_X/\omega_0, \omega_2 = \omega_Y/\omega_0, \omega_d = \Omega_d/\omega_0, \gamma_1 = \gamma_X/\gamma, \gamma_2 = \gamma_Y/\gamma, \alpha = \alpha_X d_0/\omega_0\gamma, \beta = \beta_Y d_0/\omega_0\gamma$ and $f_x = F_X/\omega_0 d_0 \gamma$.

The method of multiple scales, as presented by Nayfeh [43], can be employed to describe the response and we can obtain

$$2i\omega_1 A' + \gamma_1 i\omega_1 A + \alpha B\bar{A} \exp(i\sigma_2 T_1)$$
$$- \frac{f_x}{2} \exp[i(\sigma_1 T_1 + \tau)] = 0,$$
$$2i\omega_2 B' + \gamma_2 i\omega_2 B + \beta A^2 \exp(-i\sigma_2 T_1) = 0, \tag{A3}$$

where multiple times scales defined as $T_0 = t, T_1 = \varepsilon t$. A and B can also be written in the form of in-phase and quadrature components as $A = 0.5(p_1 - iq_1)e^{iv_1 T_1}$ and $B = 0.5(p_2 - iq_2)e^{iv_2 T_1}$ where $v_1 = \sigma_1$, $v_2 = 2\sigma_1 - \sigma_2$.

Substituting A, B into Eq. (A3) and separating the real and imaginary parts, we obtain

$$p'_1 = -v_1 q_1 - \frac{1}{2}\gamma_1 p_1 - \Lambda_1 (p_1 q_2 - p_2 q_1) + \frac{f_x}{2\omega_1} \cos\tau,$$
$$q'_1 = v_1 p_1 - \frac{1}{2}\gamma_1 q_1 - \Lambda_1 (p_1 p_2 + q_1 q_2) + \frac{f_x}{2\omega_1} \sin\tau,$$
$$p'_2 = -v_2 q_2 - \frac{1}{2}\gamma_2 p_2 + 2\Lambda_2 p_1 q_1,$$
$$q'_2 = v_2 p_2 - \frac{1}{2}\gamma_2 q_2 - \Lambda_2 (p_1^2 - q_1^2), \tag{A4}$$

where $\Lambda_1 = \alpha/4\omega_1, \Lambda_2 = \beta/4\omega_1$. If we define $y = [p_1, q_1, p_2, q_2]^T$, the equations can be regarded as the basic equations of nonlinear coupling model in the vector form of $y' = f(y)$. Under this circumstance, the final solutions can be expressed as

$$x \approx x_0 = p_1 \cos\omega_1' t + q_1 \sin\omega_1' t,$$
$$y \approx y_0 = p_2 \cos\omega_2' t + q_2 \sin\omega_2' t, \tag{A5}$$

where $\omega_1' = \omega_1 + \varepsilon v_1 = \omega_d, \omega_2' = \omega_2 + \varepsilon v_2 = 2\omega_d$. Furthermore, p and q can be obtained from the in-phase and quadrature components of the modal vibrations by the demodulation of detection signal in experiments.

2. Theoretical analysis of M-shaped responses and stability determination

It is more convenient to find fixed points and obtain the amplitude-frequency response of this nonlinear coupling model by expressing A and B in the polar form as $A = 0.5a_1 e^{i\theta_1}$, $B = 0.5a_2 e^{i\theta_2}$, where a_n and θ_n are the amplitudes and phases of the two modes.

Substituting into Eq. (A3) and separating real and imaginary parts, we obtain

$$a'_1 = -\frac{\gamma_1}{2} a_1 - \frac{\alpha a_1 a_2 \sin\delta_2}{4\omega_1} + \frac{f_x \sin\delta_1}{2\omega_1},$$
$$a'_2 = -\frac{\gamma_2}{2} a_2 + \frac{\beta a_1^2 \sin\delta_2}{4\omega_2},$$
$$\theta_1' = \frac{\alpha a_2 \cos\delta_2}{4\omega_1} - \frac{f_x \cos\delta_1}{2\omega_1 a_1},$$
$$\theta_2' = \frac{\beta a_1^2 \cos\delta_2}{4\omega_2 a_2}, \tag{A6}$$

where $\delta_1 = \sigma_1 T_1 - \theta_1 + \tau, \delta_2 = \theta_2 - 2\theta_1 + \sigma_2 T_1$, is the driving phase and set to zero in most cases. The fixed points of Eq. (A6) correspond to the constant value of a_1, a_2, δ_1, and δ_2, namely $a_1' = a_2' = 0$ and $\delta_1' = \sigma_1 - \theta_1' = 0, \delta_2' = \theta_2' - 2\theta_1' + \sigma_2 = 0$.

Substituting into Eq. (A6), a polynomial equation of a_1 can be derived as

$$\hat{a}_1^6 + 2\left(\frac{\gamma_1\gamma_2}{4} - v_1 v_2\right)\hat{a}_1^4 + {\chi_1}^2{\chi_2}^2\hat{a}_1^2 - {\chi_2}^2\frac{\Lambda_1\Lambda_2}{4{\omega_1}^2}f_x = 0, \tag{A7}$$

where $\chi_n^2 = v_n^2 + \gamma_n^2/4$, $v_1 = \sigma_1$, $v_2 = 2\sigma_1 - \sigma_2$, $\Lambda_1 = \alpha/4\omega_1$, $\Lambda_2 = \beta/4\omega_1$, and $\hat{a}_1 = \Lambda_1\Lambda_2 a_1$.

With the modification of parameter σ_1, the M-shaped responses can be simulated by calculating the amplitude a_1 of Eq. (A7). Besides, the stability of the these solutions can be determined from the Jacobian matrix of Eq. (A4) as shown in Eq. (A8). The transforms between two forms of expression are $p_1 = a_1\cos(\tau - \delta_1)$, $q_1 = a_1\sin(\tau - \delta_1)$ and $p_2 = a_2\cos\delta_2$, $q_2 = a_2\sin\delta_2$.

$$f_{\mathrm{Jac}} = \begin{bmatrix} -0.5\gamma_1 + \Lambda_1 q_2 & -v_1 - \Lambda_1 p_2 & -\Lambda_1 q_1 & \Lambda_1 p_1 \\ v_1 - \Lambda_1 p_2 & -0.5\gamma_1 - \Lambda_1 q_2 & -\Lambda_1 p_1 & -\Lambda_1 q_1 \\ 2\Lambda_2 q_1 & 2\Lambda_2 p_1 & -0.5\gamma_2 & -v_2 \\ -2\Lambda_2 p_1 & 2\Lambda_2 q_1 & v_2 & -0.5\gamma_2 \end{bmatrix}. \tag{A8}$$

Substituting them into Eq. (A8), these solutions of Eq. (A7) can be identified as stable fixed points when all the eigenvalues of the Jacobian matrix have the negative real parts. Otherwise, the solutions are unstable solutions. In the simulation results of M-shaped responses, the stable and unstable points are labeled as blue and red colors, respectively. Particularly, the Hopf bifurcations can also be identified when two complex conjugate eigenvalues cross the imaginary axis into the right half of the complex plane.

3. Model parameters' matching

To carry out the numerical simulation, the parameters identified from two modes under the condition of internal resonance are listed in Table I. In particular, the parameters α_X and β_Y are obtained from the fitting between the simulation and experimental results. In addition, the differential driving force $F_X\cos(\Omega_d t^* + \tau)$ is applied by electrostatic actuation, which can be expressed as $F_X = 2A_d\varepsilon_0 V_{\mathrm{dc}} V_d/d_0^2 m_X$.

The bias voltage V_{dc} is mainly used to adjust strength of internal resonance σ_2 in the experiments. As illustrated in Fig. 6, the resonant frequencies of two modes have different frequency shifts due to the negative electrostatic stiffness when the bias voltage V_{dc} is modified. Besides, the V_d is mainly utilized to tune the driving force F_1 applied on the resonator and control the amplitudes of two mechanical modes.

TABLE I. Model coefficients and structural parameters obtained from the experiments.

Parameter	Meaning	Value
$\omega_X = 2\pi f_1$	Resonant frequency of mode I	$2\pi \cdot 151.8513$ kHz
$\omega_Y = 2\pi f_2$	Resonant frequency of mode II	$2\pi \cdot 303.7033$ kHz
γ_X	damping rate of mode I	$2\pi \cdot 2.1387$ Hz
γ_Y	damping rate of mode II	$2\pi \cdot 2.0251$ Hz
α_X	Nonlinear coupling coefficient	1.1958×10^{15} m^{-1}s^{-2}
β_Y	Nonlinear coupling coefficient	2.5264×10^{15} m^{-1}s^{-2}
A_d	Area of capacitance	5.1×10^{-9} m^2
d_0	Gap of capacitance	1.5×10^{-6} m
m_X	Equivalent mass of resonator	5.8×10^{-9} kg

APPENDIX B: THEORETICAL ANALYSIS OF GENERATION MECHANISM

1. Generation of frequency comb from the amplitude-and-phase modulation

Between two Hopf bifurcations, the periodic behavior of coherent energy transfer results in the amplitude and phase modulation of two mechanical modes, which can be

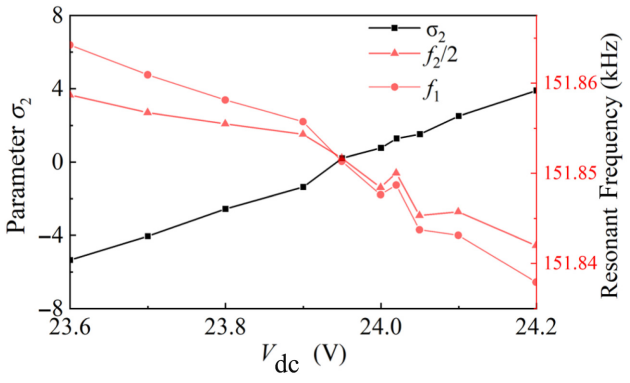

FIG. 6. Strength of internal resonance σ_2 detuned by V_{dc}.

expanded by the Fourier series in equation.

$$x(t) = a(t)\cos[\omega_d t + \theta(t)],$$
$$a(t) = A_0 + \sum_{N=1}^{\infty} A_N \sin(N\Delta\omega t + \varphi_N),$$
$$\theta(t) = \theta_0 + \sum_{n=1}^{\infty} \theta_n \sin(n\Delta\omega t + \lambda_n), \tag{B1}$$

where $\Delta\omega = 2\epsilon\pi/T_{\mathrm{LC}}$, T_{LC} represents the period of coherent energy transfer.

According to the Jacobi-Anger identity and neglecting the higher order, modal vibration is $x(t) = A_0 \sum_{k=-\infty}^{+\infty} (-1)^k J_k(\theta_1) \cos[(\omega + k\Delta\omega)t + \vartheta_0] + \frac{1}{2}\sum_{N=1}^{\infty}\sum_{k=-\infty}^{+\infty} (-1)^k A_N J_k(\theta_1)\{\sin[[\omega + (k+N)\Delta\omega]t + \vartheta_0 + \varphi_N] - \sin[[\omega + (k-N)\Delta\omega]t + \vartheta_0 - \varphi_N]\}$ where J_i represents the ith-order Bessel function and $\vartheta_0 = \theta_0 + k\lambda_1$. This equation indicates that the modal vibration contains a series of sidebands of $\omega + m\Delta\omega$ symmetric distributed around the center resonant frequency ω. To obtain the amplitude of mth comb of PFC, combine all the $\omega + m\Delta\omega$ components together and we can obtain $x_{\omega+m\Delta\omega}(t) = A_0 J_m(\theta_1)\cos[(\omega + m\Delta\omega)t + \theta_0 + m\lambda_1 + m\pi] + \frac{1}{2}\sum_{N=1}^{\infty} A_N J_{m-N}(\theta_1)\sin[[\omega + m\Delta\omega]t + \theta_1] - \frac{1}{2}\sum_{N=1}^{\infty} A_N J_{m+N}(\theta_1)\sin[[\omega + m\Delta\omega]t + \theta_2]$ where $\theta_1 = \theta_0 + (m-N)\lambda_1 + (m-N)\pi + \varphi_N$ and $\theta_2 = \theta_0 + (m+N)\lambda_1 + (m+N)\pi - \varphi_N$.

It can be simplified as follows:

$$x(t) = \sum_{m=-\infty}^{\infty} x_{\omega+m\Delta\omega}(t) = \sum_{m=-\infty}^{\infty} \Gamma_m \cos((\omega_d + m\Delta\omega)t + \Theta_m), \tag{B2}$$

where $\Gamma_m = \sqrt{U_m^2 + V_m^2}$, $\Theta_m = \theta_0 + m\lambda_1 + m\pi + \arctan(V_m/U_m)$ are the amplitude and phase of mth comb tooth. The U_m and V_m can be expressed as

$$U_m = A_0 J_m(\theta_1) - \frac{1}{2}\sum_{N=1}^{\infty} A_N\,(J_{m+N}(\theta_1) + J_{m-N}(\theta_1))\sin\phi_N,$$
$$V_m = \frac{1}{2}\sum_{N=1}^{\infty} A_N\,[J_{m+N}(\theta_1) - J_{m-N}(\theta_1)]\cos\phi_N,$$
$$\phi_N = N\lambda_1 + N\pi - \varphi_N. \tag{B3}$$

Equation (B2) indicates that the amplitude and phase modulation of mechanical modes due to coherent energy transfer generates a series of discrete, equally spaced elements in the spectrum, namely the phononic frequency combs.

2. Calculation of PFC from in-phase and quadrature components of experimental results

In this paper, we want to illustrate the generation mechanism form the modulation of mechanical modes by coherent energy transfer. It has been clearly expressed in Eq. (B2) and the simulation is also carried out by sorting and combining all the amplitudes of the same comb tooth together to verify the mechanism. This method is effective in the illustration of generation mechanism but it is not convenient and accurate for the calculation, especially for a great deal of simulation work in the evolution process. Hence, the method of calculating PFC from in-phase and quadrature components is proposed to carry out the simulation effectively. The modal vibration can also be expressed in the form of in-phase and quadrature components $x(t) = p_1(t)\cos\omega_d t + q_1(t)\sin\omega_d t$. The periodic modulation of the coherent energy allows $p_1(t)$ and $q_1(t)$ to be expanded by the Fourier series as follows:

$$p_1(t) = a_{0p} + \sum_{N=1}^{\infty} a_{Np}\cos N\Delta\omega t + \sum_{N=1}^{\infty} b_{Np}\sin N\Delta\omega t,$$
$$q_1(t) = a_{0q} + \sum_{N=1}^{\infty} a_{Nq}\cos N\Delta\omega t + \sum_{N=1}^{\infty} b_{Nq}\sin N\Delta\omega t. \tag{B4}$$

Hence, the modal vibration can be illustrated as $x(t) = a_{0p}\cos\omega t + a_{0q}\sin\omega t + \sum_{N=1}^{\infty}\left[\begin{matrix}(a_{Np}\cos N\Delta\omega t + b_{Np}\sin N\Delta\omega t)\cos\omega t \\ +(a_{Nq}\cos N\Delta\omega t + b_{Nq}\sin N\Delta\omega t)\sin\omega t\end{matrix}\right]$.

For each item of N, it contains two sidebands with frequencies of $\omega \pm N\omega_1$.

$(a_{Np}\cos N\Delta\omega t + b_{Np}\sin N\Delta\omega t)\cos\omega t + (a_{Nq}\cos N\Delta\omega t + b_{Nq}\sin N\Delta\omega t)\sin\omega t = \frac{1}{2}\sqrt{U_N + V_N}\cos(\omega t + N\Delta\omega t + \Phi_{N+}) + \frac{1}{2}\sqrt{U_N - V_N}\cos(\omega t - N\Delta\omega t + \Phi_{N-})$ where $U_N = a_{Np}^2 + b_{Np}^2 + a_{Nq}^2 + b_{Nq}^2$, $V_N = 2a_{Nq}b_{Np} - a_{Np}b_{Nq}$, $\Phi_{N+} = \arctan(-b_{Np} + a_{Nq}/a_{Np} - b_{Nq})$, $\Phi_{N-} = \arctan(--b_{Np} + a_{Nq}/a_{Np} + b_{Nq})$.

Therefore, the calculation of frequency comb can be concluded as follows:

$$A_\omega = \sqrt{a_{0p}^2 + a_{0q}^2},$$
$$A_{\omega+N\Delta\omega} = \frac{1}{2}\sqrt{U_N + V_N}, A_{\omega-N\Delta\omega} = \frac{1}{2}\sqrt{U_N - V_N}. \quad \text{(B5)}$$

APPENDIX C: THEORETICAL ANALYSIS OF EVOLUTION

1. Simulation method for evolution

The generation of phononic frequency comb is based on the existence of the limit cycle and its evolution comes from the modification of the limit cycles. After calculating the four Lyapunov exponents of Eq. (A4) with the standard methods from Ref. [44], the regions of limit cycles and chaos can be identified and the bifurcation points can also be located. Apart from the chaotic region and bifurcation points, the continuous evolution laws of residual regions can be simulated. The algorithm of simulating the evolution laws of coherent energy transfer in a certain subregion is based on the shooting method and the continuation method to analyze the modification of limit cycles. The shooting method will calculate the shape and period of the limit cycle in the beginning of the subregion, and the continuation method will continue to search for the following limit cycles with the modification of driving frequency.

The periodic solution of the nonlinear systems $y' = f(y)$ is found by solving the two-point boundary value problem. The orbit can be constructed by integrating with these initial conditions for one period and iterated by Eq. (C1) to obtain the shape and period of limit cycles [45].

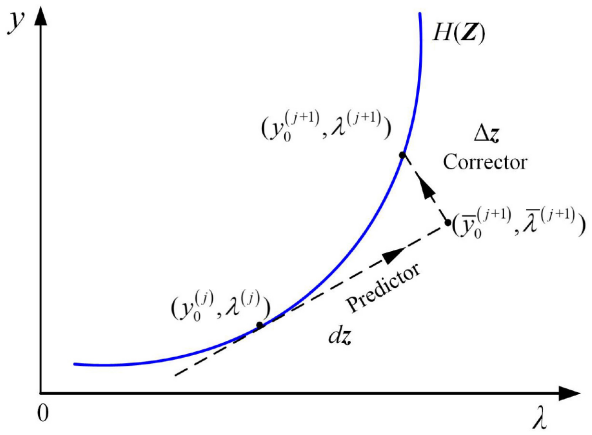

FIG. 7. Predictor-corrector principle of continuation method.

$$\begin{bmatrix} \Delta y_0 \\ \Delta T \end{bmatrix} = \begin{bmatrix} (\Phi_{T^{(i)}} - I) & f\left[\varphi\left(y_0^{(i)}; T^{(i)}\right)\right] \\ f\left(y_0^{(i)}\right)^T & 0 \end{bmatrix}^{-1} \times \begin{bmatrix} -\left(\varphi\left(y_0^{(i)}; T^{(i)}\right) - y_0^{(i)}\right) \\ 0 \end{bmatrix}, \quad \text{(C1)}$$

where i is the numbers of iteration and $\Phi_{T^{(i)}}, \varphi\left(y_0^{(i)}; T^{(i)}\right)$ are the monodromy matrix and solution flow, respectively,

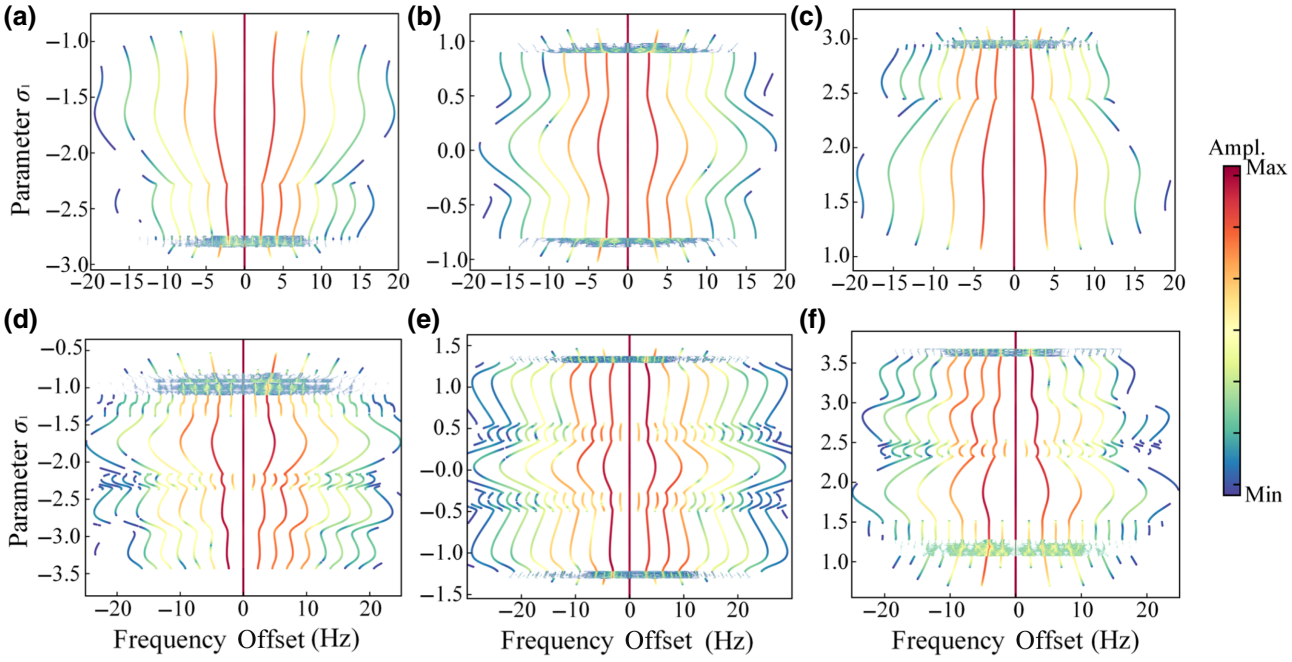

FIG. 8. Simulation results of the PFCs' evolution under different σ_2 and f_x. (a) $\sigma_2 = -2.55, f_x = 0.11$. (b) $\sigma_2 = 0.21, f_x = 0.11$. (c) $\sigma_2 = 2.5, f_x = 0.11$. (d) $\sigma_2 = -2.55, f_x = 0.17$. (e) $\sigma_2 = 0.21, f_x = 0.17$. (f) $\sigma_2 = 2.5, f_x = 0.17$.

which can be calculated by numerical integration. After several iterations, the shape and period of limit cycle will be confirmed if the value reaches the convergence conditions.

The predictor-corrector principle is introduced as the continuation method as shown in Fig. 7. The predictor calculates the predicting point by finding $d\mathbf{Z}$, which is tangent to the branch of $H(Z)$ and keeps a fixed step δ, as shown in Eq. (C2), which is called arclength continuation [36]. According to the Newton-Raphson algorithm, the correcting process is similar to the shooting method by arranging $\Delta\lambda$ to be zero [46].

$$\|dZ\| = ds = \delta, \quad \frac{dy_k}{ds} = 0$$
$$\left[\left(\Phi_{T^{(j)}} - I\right) \quad f\left(\varphi\left(y_0^{(j)}; T^{(j)}; \lambda^{(j)}\right)\right) \quad \frac{\partial y}{\partial \lambda^{(j)}}\right] \times \begin{bmatrix} dy_0 \\ dT \\ d\lambda \end{bmatrix} = 0. \tag{C2}$$

2. Simulation results of the frequency comb's evolution

After calculating four Lyapunov exponents and removing the chaotic region, the evolution law of the remaining part can be simulated efficiently by combining the shooting method and continuation method above together. The evolution of PFCs is simulated under different strength of internal resonance and driving force by adjusting the parameters σ_2 and σ_1, respectively, to reveal the evolution mechanism of experiments. As illustrated in Fig. 8, the simulation results are consistent with the experimental results in the paper.

[1] T. Udem, R. Holzwarth, and T. W. Hänsch, Optical frequency metrology, Nature **416**, 233 (2002).

[2] P. Del'Haye, A. Schliesser, O. Arcizet, T. Wilken, R. Holzwarth, and T. J. Kippenberg, Optical frequency comb generation from a monolithic microresonator, Nature **450**, 1214 (2007).

[3] S. A. Diddams, L. Hollberg, and V. Mbele, Molecular fingerprinting with the resolved modes of a femtosecond laser frequency comb, Nature **445**, 627 (2007).

[4] T. J. Kippenberg, R. Holzwarth, and S. A. Diddams, Microresonator-based optical frequency combs, Science **332**, 555 (2011).

[5] Z. L. Newman, V. Maurice, T. Drake, J. R. Stone, T. C. Briles, D. T. Spencer, C. Fredrick, Q. Li, D. Westly, and B. R. Ilic, *et al.*, Architecture for the photonic integration of an optical atomic clock, Optica **6**, 680 (2019).

[6] S. B. Papp, K. Beha, P. Del'Haye, F. Quinlan, H. Lee, K. J. Vahala, and S. A. Diddams, Microresonator frequency comb optical clock, Optica **1**, 10 (2014).

[7] E. Verhagen, S. Deléglise, S. Weis, A. Schliesser, and T. J. Kippenberg, Quantum-coherent coupling of a mechanical oscillator to an optical cavity mode, Nature **482**, 63 (2012).

[8] H. Okamoto, A. Gourgout, C.-Y. Chang, K. Onomitsu, I. Mahboob, E. Y. Chang, and H. Yamaguchi, Coherent phonon manipulation in coupled mechanical resonators, Nat. Phys. **9**, 480 (2013).

[9] E. Saglamyurek, N. Sinclair, J. Jin, J. A. Slater, D. Oblak, F. Bussieres, M. George, R. Ricken, W. Sohler, and W. Tittel, Broadband waveguide quantum memory for entangled photons, Nature **469**, 512 (2011).

[10] T. Herr, V. Brasch, J. D. Jost, C. Y. Wang, N. M. Kondratiev, M. L. Gorodetsky, and T. J. Kippenberg, Temporal solitons in optical microresonators, Nat. Photon. **8**, 145 (2014).

[11] P. Marin-Palomo, J. N. Kemal, M. Karpov, A. Kordts, J. Pfeifle, M. H. Pfeiffer, P. Trocha, S. Wolf, V. Brasch, and M. H. Anderson, *et al.*, Microresonator-based solitons for massively parallel coherent optical communications, Nature **546**, 274 (2017).

[12] T. J. Kippenberg, A. L. Gaeta, M. Lipson, and M. L. Gorodetsky, Dissipative Kerr solitons in optical microresonators, Science **361**, 567 (2018).

[13] B. Shen, L. Chang, J. Liu, H. Wang, Q.-F. Yang, C. Xiang, R. N. Wang, J. He, T. Liu, and W. Xie, *et al.*, Integrated turnkey soliton microcombs, Nature **582**, 365 (2020).

[14] J. Liu, H. Tian, E. Lucas, A. S. Raja, G. Lihachev, R. N. Wang, J. He, T. Liu, M. H. Anderson, and W. Weng, *et al.*, Monolithic piezoelectric control of soliton microcombs, Nature **583**, 385 (2020).

[15] J. Szabados, D. N. Puzyrev, Y. Minet, L. Reis, K. Buse, A. Villois, D. V. Skryabin, and I. Breunig, Frequency Comb Generation via Cascaded Second-Order Nonlinearities in Microresonators, Phys. Rev. Lett. **124**, 203902 (2020).

[16] L. Cao, D. Qi, R. Peng, M. Wang, and P. Schmelcher, Phononic Frequency Combs Through Nonlinear Resonances, Phys. Rev. Lett. **112**, 075505 (2014).

[17] A. Ganesan, C. Do, and A. Seshia, Phononic Frequency Comb via Intrinsic Three-Wave Mixing, Phys. Rev. Lett. **118**, 033903 (2017).

[18] I. Mahboob, Q. Wilmart, K. Nishiguchi, A. Fujiwara, and H. Yamaguchi, Tuneable electromechanical comb generation, Appl. Phys. Lett. **100**, 113109 (2012).

[19] X. Zhou, C. Zhao, D. Xiao, J. Sun, G. Sobreviela, D. D. Gerrard, Y. Chen, I. Flader, T. W. Kenny, and X. Wu, *et al.*, Dynamic modulation of modal coupling in microelectromechanical gyroscopic ring resonators, Nat. Commun. **10**, 1 (2019).

[20] A. Ganesan, C. Do, and A. Seshia, Excitation of coupled phononic frequency combs via two-mode parametric three-wave mixing, Phys. Rev. B **97**, 014302 (2018).

[21] D. A. Czaplewski, C. Chen, D. Lopez, O. Shoshani, A. M. Eriksson, S. Strachan, and S. W. Shaw, Bifurcation Generated Mechanical Frequency Comb, Phys. Rev. Lett. **121**, 244302 (2018).

[22] G. Gobat, L. Guillot, A. Frangi, B. Cochelin, and C. Touzé, Backbone curves, Neimark-Sacker boundaries and appearance of quasi-periodicity in nonlinear oscillators: Application to 1:2 internal resonance and frequency combs in MEMS, Meccanica **56**, 1937 (2021).

[23] G. Gobat, V. Zega, P. Fedeli, L. Guerinoni, C. Touzé, and A. Frangi, Reduced order modelling and experimental validation of a MEMS gyroscope test-structure exhibiting 1:2 internal resonance, Sci. Rep. **11**, 1 (2021).
[24] D. Antonio, D. H. Zanette, and D. López, Frequency stabilization in nonlinear micromechanical oscillators, Nat. Commun. **3**, 1 (2012).
[25] C. Chen, D. H. Zanette, D. A. Czaplewski, S. Shaw, and D. López, Direct observation of coherent energy transfer in nonlinear micromechanical oscillators, Nat. Commun. **8**, 1 (2017).
[26] J. Sun, H. Zhang, D. Chen, M. Pandit, G. Sobreviela, D. Xiao, M. Zhuo, D. D. Gerrard, R. Kwon, and G. Vukasin, *et al.*, in *2020 IEEE 33rd International Conference on Micro Electro Mechanical Systems (MEMS)* (IEEE, 2020), p. 769.
[27] G. Sobreviela, C. Zhao, M. Pandit, C. Do, S. Du, X. Zou, and A. Seshia, Parametric noise reduction in a high-order nonlinear MEMS resonator utilizing its bifurcation points, J. Microelectromech. Syst. **26**, 1189 (2017).
[28] R. Kubena, W. Wall, J. Koehl, and R. Joyce, Phononic comb generation in high-Q quartz resonators, Appl. Phys. Lett. **116**, 053501 (2020).
[29] S. Houri, D. Hatanaka, M. Asano, R. Ohta, and H. Yamaguchi, Limit cycles and bifurcations in a nonlinear MEMS resonator with a 1:3 internal resonance, Appl. Phys. Lett. **114**, 103103 (2019).
[30] I. Mahboob, R. Dupuy, K. Nishiguchi, A. Fujiwara, and H. Yamaguchi, Hopf and period-doubling bifurcations in an electromechanical resonator, Appl. Phys. Lett. **109**, 073101 (2016).
[31] L. Bakemeier, A. Alvermann, and H. Fehske, Route to Chaos in Optomechanics, Phys. Rev. Lett. **114**, 013601 (2015).
[32] F. Monifi, J. Zhang, Ş. K. Özdemir, B. Peng, Y.-x. Liu, F. Bo, F. Nori, and L. Yang, Optomechanically induced stochastic resonance and chaos transfer between optical fields, Nat. Photon. **10**, 399 (2016).
[33] D. Navarro-Urrios, N. E. Capuj, M. F. Colombano, P. D. García, M. Sledzinska, F. Alzina, A. Griol, A. Martínez, and C. M. Sotomayor-Torres, Nonlinear dynamics and chaos in an optomechanical beam, Nat. Commun. **8**, 1 (2017).
[34] R. Karabalin, M. Cross, and M. Roukes, Nonlinear dynamics and chaos in two coupled nanomechanical resonators, Phys. Rev. B **79**, 165309 (2009).
[35] T. S. Parker and L. Chua, *Practical Numerical Algorithms for Chaotic Systems* (Springer Science & Business Media, New York, 2012).
[36] A. H. Nayfeh and B. Balachandran, *Applied Nonlinear Dynamics: Analytical, Computational, and Experimental Methods* (John Wiley & Sons, Weinheim, 2008).
[37] A. Ganesan and A. Seshia, in *2018 European Frequency and Time Forum (EFTF)* (IEEE, 2018), p. 6.
[38] A. Ganesan and A. Seshia, Resonance tracking in a micromechanical device using phononic frequency combs, Sci. Rep. **9**, 1 (2019).
[39] J. Riemensberger, A. Lukashchuk, M. Karpov, W. Weng, E. Lucas, J. Liu, and T. J. Kippenberg, Massively parallel coherent laser ranging using a soliton microcomb, Nature **581**, 164 (2020).
[40] K. Stannigel, P. Komar, S. Habraken, S. Bennett, M. D. Lukin, P. Zoller, and P. Rabl, Optomechanical Quantum Information Processing with Photons and Phonons, Phys. Rev. Lett. **109**, 013603 (2012).
[41] L. Wang and B. Li, Thermal Logic Gates: Computation with Phonons, Phys. Rev. Lett. **99**, 177208 (2007).
[42] L. Bu, E. Arroyo, and A. A. Seshia, Frequency combs: in *2021 21st International Conference on Solid-State Sensors, Actuators and Microsystems (Transducers)* (IEEE, 2021), p. 136.
[43] A. H. Nayfeh and D. T. Mook, *Nonlinear Oscillations* (John Wiley & Sons, Weinheim, 2008).
[44] A. Wolf, J. B. Swift, H. L. Swinney, and J. A. Vastano, Determining lyapunov exponents from a time series, Phys. D: Nonlinear Phenom. **16**, 285 (1985).
[45] T. Aprille and T. Trick, A computer algorithm to determine the steady-state response of nonlinear oscillators, IEEE Trans. Circuit Theory **19**, 354 (1972).
[46] R. Seydel, *Practical Bifurcation and Stability Analysis* Vol. 5 (Springer Science & Business Media, New York, 2009).